Water Air Soil Pollut (2025) 236:835
https://doi.org/10.1007/s11270-025-08474-1

Sustainable Mn-doped ZnO Nanoparticles as an Efficient Cathode Catalyst for Enhanced ORR and Photocatalytic Dye Degradation in Microbial Fuel Cells

Soumyajit Chandra · Soumya Pandit · Aarti Gupta · Mohit Sahni · Mithul Rajeev · Elvis Fosso-Kankeu

Received: 26 May 2025 / Accepted: 8 August 2025 / Published online: 2 October 2025
© The Author(s) 2025

Abstract In this study, *Crocus sativus* plant extract was employed in the synthesis of manganese-doped ZnO (Mn-doped ZnO) nanoparticles, which served as cathode catalysts in a Microbial Fuel Cell (MFC) for enhanced oxygen reduction reaction (ORR) and photocatalytic dye degradation. X-ray diffraction (XRD) confirmed the wurtzite hexagonal structure of ZnO, with minor peak shifts confirming successful Mn doping. UV–Vis spectroscopy revealed narrowed bandgap, enhancing visible light absorption. Fourier Transform Infrared (FTIR) spectroscopy confirmed Zn–O and Mn–O bonding. High-Resolution Transmission Electron Microscopy (HRTEM) analysis revealed well-defined nanoparticles though with slight agglomeration at higher Mn concentrations. Photocatalytic testing achieved 96.10% crystal violet degradation with 6% Mn-doped ZnO. MFC performance evaluated via polarization study, Electrochemical Impedance Spectroscopy (EIS), Linear Sweep Voltammetry (LSV), and biofouling study. MFC performance analysis showed that Mn-doped ZnO at 2 mg/cm^2 achieved a maximum volumetric power density of 12.51 W/m^3. Mn-doped ZnO exhibited Pt-comparable cost-effective performance, highlighting its potential as an efficient and eco-friendly cathode catalyst for MFCs and photocatalysis.

Keywords Microbial Fuel Cell · ORR · Manganese doped ZnO · Photocatalysis · Cathode catalyst

Soumyajit Chandra and Soumya Pandit both authors have equal contributions to this work.

S. Chandra · S. Pandit
Bio-Positive Lab, Department of Life Sciences, Sharda University, Greater Noida, Uttar Pradesh 201310, India

A. Gupta · M. Sahni (✉)
Advanced Material Research Laboratory, Department of Physics, Sharda University, Greater Noida, Uttar Pradesh 201310, India
e-mail: mohit.sahni@sharda.ac.in

M. Rajeev
Center for Global Health Research, Saveetha Medical College and Hospital, Saveetha Institute of Medical and Technical Sciences (SIMATS), Chennai 602105, Tamil Nadu, India

E. Fosso-Kankeu (✉)
Department of Metallurgy, Faculty of Engineering and the Built Environment, University of Johannesburg, Johannesburg, South Africa
e-mail: elvisfosso.ef@gmail.com

1 Introduction

Through the metabolic activity of electroactive bacteria, Microbial Fuel Cells (MFCs), directly transform chemical energy generated from organic substrates into electrical power (Lv et al., 2025). MFCs have attracted serious attention as they can treat wastewater simultaneously while generating renewable energy. Nevertheless, the technological utilization of MFCs is still restricted by the comparatively low power

density, mainly caused by the slow oxygen reduction reaction (ORR) at the cathode. Hence, the research on highly active and inexpensive cathode catalysts is critical for improving the efficiency of MFCs (Capellán-Pérez et al., 2014; Chenchouni et al., 2024; Pandit & Das, 2018; Sahni et al., 2024; Zhang et al., 2025).

Power output is determined mainly by the electrodes used and the oxidation–reduction at the electrodes (Bezzeghoud et al., 2024; Gadipelly et al., 2014; Kumar et al., 2019; Raizada et al., 2020; Subha et al., 2019).. The ORR is a critical process occurring at the cathode of a fuel cell, significantly influencing overall operation. Because of its effectiveness and better electrocatalytic performance, platinum (Pt) has lately been used as a catalyst to improve ORR on the cathode surface of MFCs. Nonetheless, due to its high expense, platinum is unsuitable for commercial microbial fuel cell applications. Consequently, it catalyzes the development of further inexpensive catalysts, such as cathode catalysts made of cadmium gallate, titanium oxide, etc. (Çiner et al., 2024; Li et al., 2017; Li et al., 2012; Raizada et al., 2020; Singh Yadav et al., 2020). In the year 2024, Sahni et al. (2024) synthesized Cadmium Gallate nanoparticles and used them as cathode catalysts in MFCs, achieving a performance that mimics the performance of an MFC with a Pt catalyst. Nonetheless, a bifunctional cathode catalyst is still required to inhibit the proliferation of unwanted microbes, hence enhancing the ORR (Sahni et al., 2024).

Among different promising alternatives, metal oxide nanomaterials, particularly zinc oxide (ZnO), have been widely explored because of their significant electrocatalytic activity, durability, and affordability. Green synthesis methods have recently gained attention as eco-friendly solutions compared to traditional chemical synthesis (Degefa et al., 2021; Faisal et al., 2021; Jayachandran et al., 2021; Karam & Abdulrahman, 2022; Kebede Urge et al., 2023; Naiel et al., 2022; Naseer et al., 2020; Raj & Lawerence, 2018; Talam et al., 2012). Among natural sources, leaf extracts have been prominently utilized for synthesizing nanoparticles owing to their high bioactive compound content (Vemuri et al., 2022).

However, despite the advantages, pristine ZnO suffers from sluggish ORR kinetics due to its wide bandgap and limited electrical conductivity. Thus, novel strategies for enhancing its electrocatalytic activity are essential. Among various strategies, transition metal doping has been a highly effective method to overcome these limitations. By doping Manganese (Mn^{2+}) on ZnO nanoparticles, it is possible to modulate the electronic structure of ZnO for enhanced electron transport and formation of oxygen vacancies that act as active sites for ORR. Mn-doping specifically brings in multiple oxidation states (Mn^{2+}/Mn^{3+}/Mn^{4+}) that engage in redox reactions actively, thus enhancing the overall electron-transfer kinetics. In addition, Mn doping reduces the bandgap of ZnO and facilitates the adsorption and reduction of oxygen molecules. These modifications synergistically improve the ORR performance, rendering Mn-doped ZnO a far more effective cathode material than undoped ZnO. In this work, the Mn-doping approach is not only used to enhance ORR activity but also to achieve visible-light-induced photocatalytic decolorization of dyes in parallel, providing an environmentally friendly and multi-functional approach towards MFC technology (Corpuz et al., 2021; Vemuri et al., 2022).

Crystal violet is a synthetic triphenylmethane dye strongly used in the textile, paper, and dyeing industries and detected in industrial wastewater mixed effluents. The extensive use of crystal violet means it is often released into the environment, and the stability of its molecular structure makes it persistent and therefore very resistant to typical biological and chemical treatment methods. Crystal violet is also known to possess toxic, mutagenic, and carcinogenic properties, even at low concentrations, contributing to ecological and public health risks upon introduction into aquatic systems. These properties make crystal violet an extremely relevant pollutant for degradation. Photocatalytic degradation using a semiconductor material like ZnO is a useful alternative, as ZnO can degrade persistent dye molecules upon being irradiated with light. Doping ZnO with Mn improves the visible light response of ZnO and the generation of reactive oxygen species. All of which makes ZnO more effective at degrading crystal violet dye (Cheng et al., 2014; Ma et al., 2025; Sharma et al., 2022; Votat et al., 2024).

So far, ZnO as a cathode catalyst in microbial fuel cells (MFC) research has shown potential, but it is constrained by poor ORR kinetics and limited multifunctionality. There are no studies yet on Mn-doped ZnO as a cathode catalyst that concurrently improve oxygen reduction reaction (ORR) and provide

photocatalytic degradation of dyes in an MFC. The novelty of this project is the use of the *Crocus sativus* leaf extract for the green synthesis of Mn-doped ZnO nanoparticles which will have dual purposes of improving MFC performance and pollutant removal. It is hypothesized that Mn will improve the electrocatalytic properties and light absorption of ZnO and thus enhance ORR activity and efficiency in degrading the crystal violet dye in the catholyte.In this research, Mn-doped ZnO was synthesized from *Crocus Sativus* leaves through a green synthesis method. The Mn-doped ZnO characterization was done employing XRD, HRTEM, UV-Spectroscopy, and XPS. Further, the doped nanoparticles were impregnated on the cathode electrode of the MFC having crystal violet as catholyte. Polarization experiments, LSV, EIS, and biofouling studies were used to assess MFC's ORR performance. Finally the dye's photocatalytic breakdown was also evaluated using UV–Vis Spectroscopy.

2 Materials and Methods

2.1 Materials

As a renewable resource for green synthesis, dried leaves of *Crocus sativus*, also called saffron, were collected from Kashmir, India. The precursor for the production of pure ZnO and Mn-doped ZnO was zinc nitrate hexahydrate ($Zn(NO_3)_2{\cdot}6H_2O$), which was acquired from Sigma-Aldrich. The precursor for manganese was manganese (II) acetate tetrahydrate ($((CH_3COO)_2Mn.4H_2O$), which was also acquired from Sigma-Aldrich. Every chemical reagent used in the experiment was of analytical quality and was used straight away, without any additional purification. Water that had been double-distilled was used during the whole synthesis process.

2.2 Preparation of Leaf Extract

To get rid of dust and other contaminants, the gathered *Crocus sativus* leaves were carefully cleaned two or three times using distilled water. The leaves were sonicated for two to three minutes to ensure thorough washing. The required amount of cleaned leaves was then mixed with distilled water and heated to 60 °C for two hours with a magnetic stirrer to extract the bioactive components. The solution was filtered into a sanitized muslin cloth to remove any solid remains when it had cooled to room temperature. Since it contained the majority of phytochemicals, the rich liquid part was collected and employed as a leaf extract throughout the manufacturing process.

2.3 Synthesis of Pure ZnO and Mn-Doped ZnO Nanoparticles

Zinc nitrate hexahydrate ($Zn(NO_3)_2{\cdot}6H_2O$) and manganese (II) acetate tetrahydrate ($((CH_3COO)_2Mn.4H_2O$) were weighted in stoichiometric proportions for doping values of $x = 0.00$, 0.02, 0.04, 0.08, and 0.1 [Zn(1-x)MnxO] to create pure and Mn-doped ZnO nanoparticles. Two distinct solutions were produced by dissolving all of these salts independently in distilled water. After that, these two solutions were combined and constantly agitated using a magnetic stirrer set at 600 rpm. Following one hour of stirring, 70–80 mL of the produced leaf extract had been added to the mixture. To facilitate the creation of nanoparticles, the mixture was then heated to 60 °C and left for two hours. To create Mn-doped ZnO nanoparticles, the dry sample was crushed into a fine powder and sintered for two hours at 500 °C. The required nanoparticle was achieved and preserved for further characterizations and applications (Kanwal et al., 2023). Nanoparticles were obtained with an average yield of approximately 80%, based on the mass of the dried nanoparticles to the theoretical maximum yield based on the zinc precursor. Batch reproducibility of these syntheses indicated the average yield and particle size had less than 3% relative standard deviation. Quality control analyses mentioned in the next section were performed to verify phase purity and composition.

2.4 Characterization Techniques

Using a variety of methods, the produced Mn-doped ZnO nanoparticles were examined for their surface, optical, magnetic, structural, and morphological features. The methods include XRD analysis carried out on "RIGAKU Ultima IV diffractometer" with operating conditions 40 kV/200 mA with CuKα radiation with a wavelength of 1.5406 Å. The samples'crystalline structure and phase composition were ascertained using XRD. The microstructure and

morphology were studied with a higher resolution by using the "high-resolution transmission electron microscope JEOL JEM 2010" running at a 200 kV accelerating voltage. The surface studies, including the elemental composition and chemical state analysis, were carried out using the XPS system connected to an "Omicron ultra-high vacuum system (ESCA 2000–125)". The XPS spectra were recorded using an "Mg-Kα" source to acquire the magnetic characterization of the Tesla Coil (12 kV, 10 mA). For vibrational modes, the Raman spectra have been obtained by a "LABRAM Horiba Jobin Yvon spectrometer" with laser energy at 532 nm working in backscattering geometry. Finally, for the optical properties of nanocrystalline samples, a Shimadzu UV–Vis-1800 spectrophotometer was utilized.

2.5 Photocatalytic Experiment

In this research work, crystal violet dye was used as the model contaminant to test the photocatalytic activity of Mn-doped ZnO. First, a suitable quantity of crystal violet dye was dissolved in distilled water in a conical flask to create a 10-ppm solution. The solution was kept in a dark environment for half an hour before the photocatalytic process was activated. For the molecules of dye and the photocatalyst to achieve adsorption–desorption equilibrium, this step was necessary. The pre-equilibration in the dark guarantees that any loss of dye concentration during the reaction can be accounted for by photocatalytic degradation and not by mere adsorption on the catalyst surface. After the dark adsorption, the solution was poured into a conical flask, and a known quantity of the ZnO and Mn-doped ZnO photocatalyst was added to individual flasks.

The catalyst particles were then evenly distributed throughout the dye solution by shaking the flask. The effectiveness of the degradation process is increased when the dye molecules and photocatalyst contact as much as possible, which is ensured by proper mixing. After uniform dispersion was attained, the flask was left under direct sunlight, which acted as the source of irradiation to stimulate the photocatalyst. The source of irradiation was direct natural sunlight. However, the sunlight intensity was not measured. Future research will include irradiance records. The experiments were performed in standard borosilicate glass conical flasks (100 mL, with a solution depth of 2-3 cm) to allow light to penetrate with consistent exposure. Control experiments were also conducted without Mn-doped ZnO. Under the photocatalytic reaction, samples were drawn at intervals of 20 min to track the degradation process. A "UV–visible spectrophotometer" was further used in the measurement of collected samples, providing absorbance values that were associated with the amount of residual dye in the solution. It was possible to assess the photocatalytic efficacy of the produced Mn-doped ZnO by measuring the reduction in absorbance with time, which indicated the extent of dye degradation.

2.6 Impregnation of Mn-doped ZnO on Cathode Electrode Surface

A sonicator was utilized to immerse the Mn-doped ZnO in distilled water. The mixture underwent sonication for three hours, after which it was moved to 0.5 ml of a 5% polyvinyl alcohol (PVA) solution, and subjected to an additional thirty minutes of sonication. A 1 molar solution of hydrochloric acid (HCl) was used to eliminate any particulate matter or foreign substances from clusters of graphite felt. The electrode pieces were first subjected to sonication for 30 min in a reservoir containing distilled H_2O to discard any residual particles. Subsequently, they were regularly cleansed in a solution comprising distilled water and 35% ethanol. Ultimately, they were placed in a muffle furnace for thermal treatment for about 30 min at a temperature of 400 °C. The cathodes were modified using Mn-doped ZnO by applying various ratios of sonicated Mn-doped ZnO from the aforementioned mixture onto a graphite felt by spraying. The cathodes were thereafter maintained at a temperature of 60 °C for the duration of one night. By using the same procedure, a pristine graphite-felt cathode was produced, without the inclusion of Mn-doped ZnO in the mixture.

2.7 Construction, Operation, and Performance Evaluation of MFCs

For this study, 5 double-chambered acrylic MFCs were utilized. The anodic and cathodic chambers of the MFCs were 1 L each. Both the "anode" and "cathode" electrodes were constructed of graphite felt and are 15 cm X 12 cm in size. The cathode electrodes were impregnated with Mn-doped Cathodes at a

concentration of 1, 1.5, 2, and 2.5 mg/cm^2. There was no cathode catalyst in the control MFC. The anode and the cathode electrodes were connected using an external wire and a 10 Ω resistor. A "Nafion membrane" was utilized as a "Proton Exchange Membrane (PEM)" within the two chambers. All the openings in the anode chamber are sealed to maintain an anaerobic environment. Lastly, an anaerobic environment was created by sparging nitrogen gas into the reactor.

As the substrate, synthetic acetate medium was used in the anode chamber. *Pseudomonas aeruginosa* PA1_NCHU was used as inoculum at a volume of 10% (v/v). In the cathode chamber, crystal violet (10 ppm) was added as catholyte. A pH of 6.5 ± 0.3 and a temperature of 35 °C were maintained in all the MFCs. The MFCs operated continuously for 30 days, with several substrate replenishment cycles once every 5–6 days. Experiments were performed in triplicates to investigate variability and reproducibility. Voltage outputs were typically stable by 5–6 days of startup operation, and remained stable between cycles of operation, demonstrating operational stability of the system. Reproducibility was considered good if the Relative Standard Deviation (RSD) was below 5% across replicates for each key performance indicator.

The polarization studies were done using a multimeter instrument. These MFCs could attain their maximum voltage by being held in open-circuit mode before the polarization research. Polarization curves were generated by measuring the ensuing voltage drop and using a"variable resistance box of range from 90 kΩ to 20 kΩ"to change the external resistance of the closed circuit at distinct elevations. Typically, it required around 8–10 min to obtain a consistent value. An electrochemical experiment was carried out with a set of three electrodes using a potentiostat (BioLogic SP150). The "reference electrode" was "Ag/AgCl", the "counter electrode" was a "platinum (Pt)" wire, and the "working electrode" was a "cathode". The −0.8 to 0.8 V potential range was covered for LSV, which was done at 2 mV/s (scan rate). EIS was carried out on the anode using the same electrode arrangement. A 5 mV amplitude sinusoidal disturbance was applied as part of the EIS. The range of frequency for the EIS ranged from 100 kHz to 1 Hz. The crystal violet dye degradation in the cathode chamber was studied using UV–Vis Spectroscopy. The biofouling study was done using "Confocal Laser Scanning Microscopy (CLSM)". The procedure of CLSM was the same as the previous study (Kumar et al., 2019).

3 Results and Discussion

3.1 Mn-doped ZnO Characterization

3.1.1 XRD Study

Figure 1 displays the XRD structures of ZnO and Mn-doped ZnO nanoparticles made using the sol–gel technique with doping concentrations of 2%, 4%, 6%, 8%, and 10%. According to JCPDS No. 36–1451 space group P63mc, the hexagonal wurtzite framework of ZnO was identified as the source of the diffraction peaks (Achouri et al., 2016; Das et al., 2023; Dhivya et al., 2022). The ZnO lattice's strong crystallinity is verified by the diffraction peaks at the "(100), (002), (101), (102), (110), (103), (200), and (112)" planes. Secondary phases for manganese oxides (e.g., MnO or MnO_2) were not detected, demonstrating the substitution of Zn^{2+} ions with Mn^{2+} ions into the ZnO lattice without creating independent phases (Das et al., 2023). The graph was drawn between relative intensity (a.u.) and diffraction angle (2θ) to compare the structural features of pure and Mn-doped ZnO samples. A consistent shift in the peak positions with increasing concentration of Mn doping was noticed due to the substitution of Mn^{2+} ions (ionic

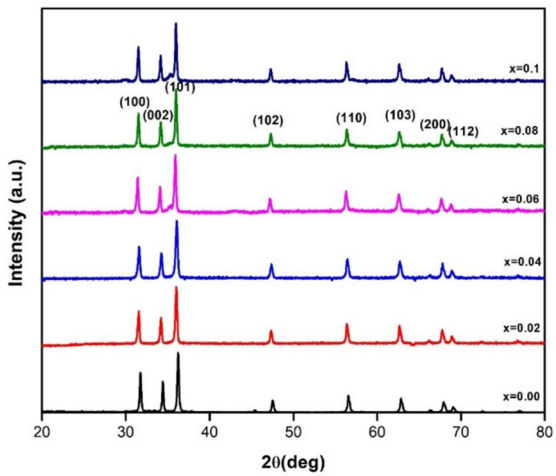

Fig. 1 XRD of ZnO & ZnO with Mn Doping [$Zn_{(1-x)}$ Mn_xO, where x = 0.00, 0.02, 0.04, 0.06, 0.08, 0.1]

radius: 0.66 Å) into the Zn^{2+} sites (ionic radius: 0.74 Å), causing lattice contraction(Akram et al., 2023; Dhivya et al., 2022; Shatnawi et al., 2016). The average size of the crystallites was determined using the Scherrer equation. In pure ZnO, the crystallite size was 38.15 nm, and it reduced to 32.72 nm for 2% Mn doping and to 28.64 nm for 4% Mn doping. These decreases in crystallite size arise because the lattice strain caused by Mn substitution is preventing crystal growth. At increased doping, the crystallite size slightly rose by 33.33 nm to 35.46 nm and 36.02 nm for 6%, 8%, and 10% Mn doping, respectively. This would be a trend owing to strain relaxation and the onset of agglomeration with increasing Mn concentrations. The maximum intensities of the XRD patterns lowered with the Mn doping concentration increasing, especially at lower doping levels (2% and 4%), showing the decrease in crystallinity as a result of lattice defects and strain introduced (Akram et al., 2023; Kanwal et al., 2023). The peak broadening at intermediate doping levels further confirms the micro-strain (Akram et al., 2023). At higher doping concentrations (8% and 10%), there was partial relaxation of the strain and minor reorganization of the lattice, leading to enhanced crystallite size and peak intensity. These findings indicate that the Mn incorporation induces strain and defects into the ZnO lattice, which affects the structural properties of the material (Kumar et al., 2016). The structural analysis proves that Mn doping considerably modifies the ZnO lattice, with the best effects being achieved at 4% doping, where the crystallite size and strain are the most significant. The material's functional characteristics, particularly its photocatalytic activity, are probably going to be impacted by these structural changes.

3.1.2 High-Resolution Transmission Electron Microscope (HRTEM)

The shape, size, and crystallinity of both the pure and the Mn-doped ZnO nanoparticles are clarified by HRTEM pictures. The pure ZnO's TEM micrographs show clumped nanoparticles (Dhivya et al., 2022; Silambarasan et al., 2024) (Fig. 2a) having dimensions between ~ 42.2 nm and 73.9 nm, and corresponding size distribution analysis verifies the average particle size of 73 nm (Fig. 2b). The SAED pattern (Fig. 2c) consists of sharp diffraction rings indexed to the (100), (002), (101), (102), and (110) planes, demonstrating a polycrystalline wurtzite structure, which is also verified by XRD (Silambarasan et al., 2024). When doped with Mn, the particle size is reduced, as indicated by the HRTEM images, where 2% Mn-doped ZnO has particle sizes ranging from ~ 21.5 nm to 35.1 nm (Fig. 2d) with an average of 33.5 nm (Fig. 2e), and comparable reductions are found in 6% Mn-doped ZnO (~ 20–28 nm, average 33 nm) (Fig. 2g, 2h) and 10% Mn-doped ZnO (~ 26.8–40.1 nm, average 38 nm) (Fig. 2j, 2k). The SAED patterns for all the Mn-doped samples (Fig. 2f, 2i, 2l) have the same polycrystalline character as the pure ZnO, which supports the lack of impurity phases, consistent with the XRD results with no extra peaks besides those of wurtzite ZnO (Silambarasan et al., 2024). The less the size of ZnO: Mn, the more it is expected to show good photocatalytic activity (Achouri et al., 2016; Kistan et al., 2024). The size reduction observed upon Mn incorporation is due to Mn ions suppressing the growth of ZnO grains, a trend which is also substantiated by XRD in terms of a systematic broadening of diffraction peaks, characteristic of smaller crystallite sizes as obtained from Scherrer's equation (Achouri et al., 2016). Additionally, the impact of Mn doping as shown by the HRTEM study is supported by the diffraction peak shift in XRD induced by lattice distortion, confirming that Mn^{2+} was successfully inserted into the ZnO structure without affecting its fundamental crystalline structure. Therefore, HRTEM coupled with XRD establishes that Mn doping successfully miniaturizes ZnO particle size while maintaining its wurtzite structure without introducing secondary phases.

3.1.3 UV–Vis Spectrophotometer

The UV–Vis absorption spectra of undoped ZnO and Mn-doped ZnO nanoparticles were measured with a wavelength of 200–900 nm to know their optical bandgap energy (E_g) (Ahmed, 2017; Akram et al., 2023; Arefi & Rezaei-Zarchi, 2012; Faisal et al., 2021; Iqbal et al., 2024; Morozov et al., 2015; Naiel et al., 2022). The bandgap energy was derived from Tauc's plot, in which $(\alpha h\nu)^2$ was correlated with photon energy (E). The bandgap values were obtained by extrapolating a linear portion of the figure to the energy axis (Arefi & Rezaei-Zarchi, 2012; Faisal et al., 2021; Morozov et al., 2015; Rahman et al., 2022). The measurements reveal that pristine ZnO

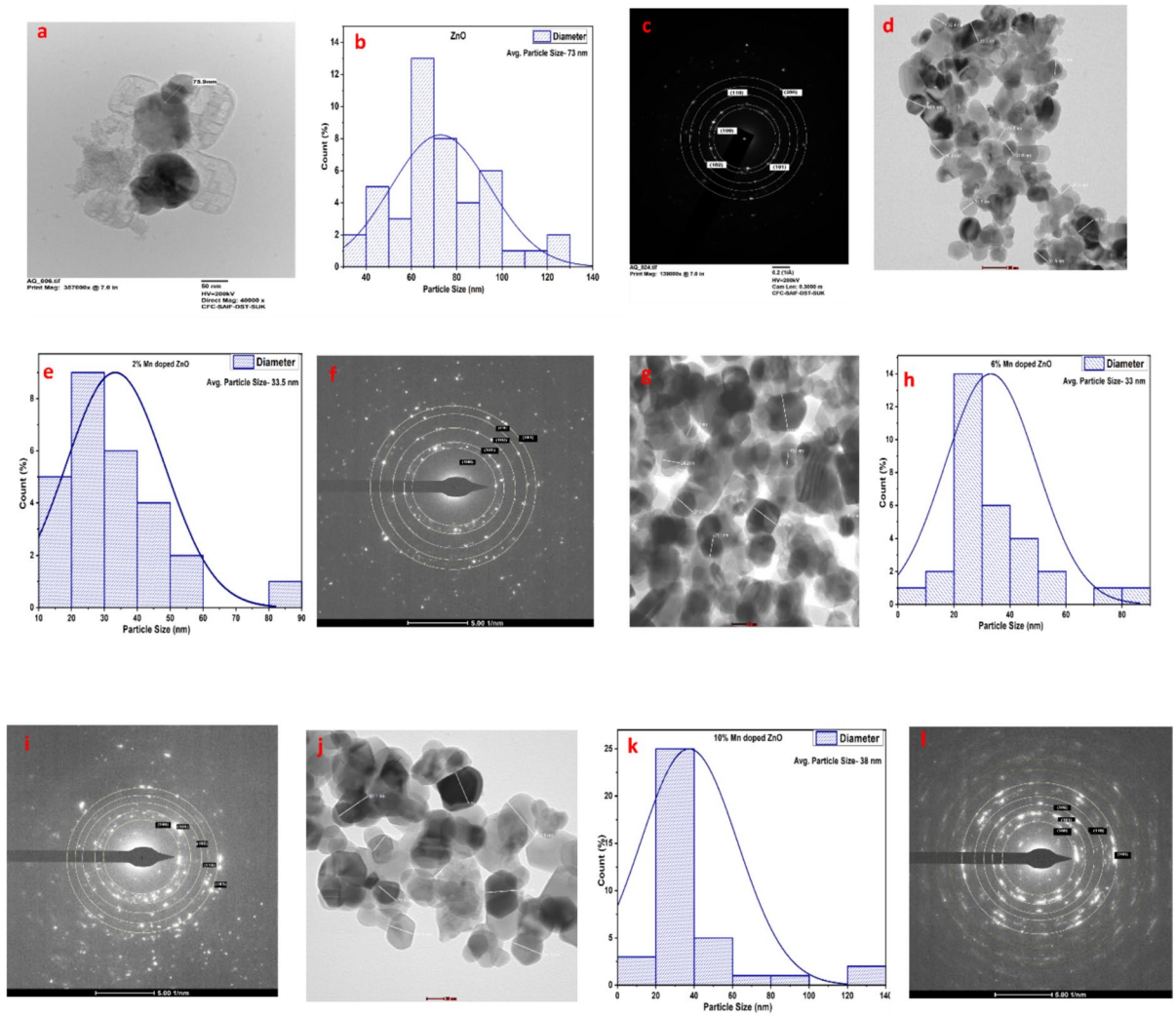

Fig. 2 **a**: HRTEM image of ZnO at 50 nm scale. **b**: Avg. Particle Size of ZnO **c**: SAED pattern of ZnO **d**: HRTEM image of ZnO with 2% Mn doping at 50 nm scale **e**: Average. Particle Size of ZnO with 2% Mn doping **f**: SAED pattern of ZnO with 2% Mn doping **g**: HRTEM image of ZnO with 6% Mn doping at 50 nm scale **h**: Avg. Particle Size of ZnO with 6% Mn doping **i**: SAED pattern of ZnO with 6% Mn doping **j**: HRTEM image of ZnO with 10% Mn doping at 50 nm scale **k**: Avg. Particle Size of ZnO with 10% Mn doping **l**: SAED pattern of ZnO with 10% Mn doping

has a bandgap of 3.33 eV (Fig. 3a), which agrees with the published bandgap of bulk ZnO (Arefi & Rezaei-Zarchi, 2012; Faisal et al., 2021; Morozov et al., 2015; Rahman et al., 2022). For Mn-doped ZnO, the bandgap varies nonlinearly, which reflects the effect of dopant incorporation on the electronic band structure of ZnO (Ahmed, 2017; Akram et al., 2023; Iqbal et al., 2024; Kumar et al., 2016).

In the 2% Mn-doped ZnO (Fig. 3b), the bandgap further reduces to 3.08 eV, indicating the insertion of mid-gap states that occur due to Mn doping. Mid-gap states represent localized impurity states within the ZnO band structure through which electronic transitions take place at low energy, hence causing a redshift in absorption (Ahmed, 2017). With increased concentration of Mn, to 4% and 6%, a slight increase of the bandgap to 3.16 eV and 3.17 eV occurs (Fig. 3c, 3 d), respectively. The Burstein-Moss effect explains this increase, in which a rise in free carrier concentration causes the lower energy states

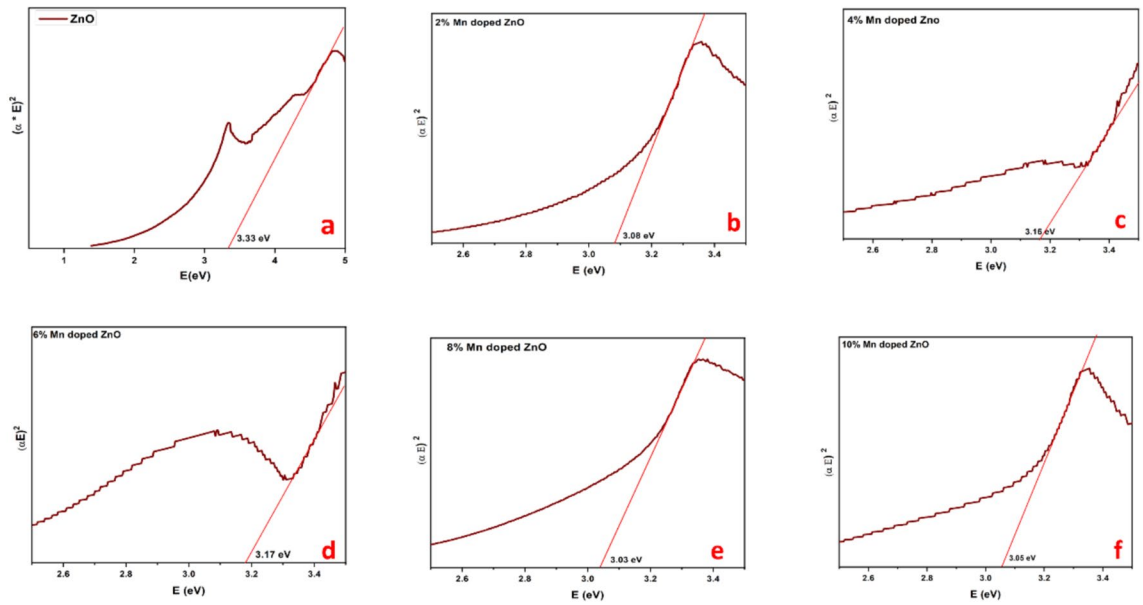

Fig. 3 **a**: UV plot of ZnO **b**: UV plot of ZnO with 2% Mn doping **c**: UV plot of ZnO with 4% Mn doping **d**: UV plot of ZnO with 6% Mn doping **e**: UV plot of ZnO with 8% Mn doping **f**: UV plot of ZnO with 10% Mn doping

of the conduction band to be filled, thereby moving the absorption edge to higher energies (Ahmed, 2017; Akram et al., 2023; P. Kumar et al., 2016; Silambarasan et al., 2024). This effect is most evident when dopant atoms provide extra free carriers, altering the charge carrier behaviour in the semiconductor. Also, the stress caused by substitution of Mn in the ZnO lattice, which is evident from XRD data, could be contributing to this bandgap widening (Achouri et al., 2016). This decrease in crystallite size is consistent with the narrowing of the bandgap observed at 4% substitution of Mn, indicating that quantum confinement effects could be at work (Arefi & Rezaei-Zarchi, 2012).

For greater concentrations of Mn of 8% and 10%, the considerable bandgap lowering is realized at values of 3.03 eV and 3.05 eV, respectively (Fig. 3e, 3f). This reduction may be attributed to the presence of extra defect states caused by excessive incorporation of Mn, creating localized states within the bandgap. These defect states allow for sub-bandgap transitions, hence leading to lowering of the effective optical bandgap (Achouri et al., 2016; Sharma et al., 2022). The disorder in the structure created by high Mn doping also contributes to this narrowed bandgap as higher defect densities and lattice strain can affect the electronic band structure (Iqbal et al., 2024). This irregularity in the observed band gap has been observed in another study where nanoparticles were synthesised by the solid-state reaction route (Sharma et al., 2022). Similarly, Kumar et al. (2016) found similar results, seeing a drop in the band gap at first followed by an increase later on. He called this pattern"bowing"in the band gap, which second-order perturbation theory theoretically explains (Kumar et al., 2016). This trend parallels the amorphization effect frequently observed in heavily doped semiconductor systems, where extra dopants cause lattice distortion and defect states, which in turn modify the electronic band structure. It can also be accounted for by elevated defect states and structural distortions, as indicated in HRTEM images wherein agglomeration and lattice defects become more significant. The association among the observed bandgap variations and XRD-established crystallite size diminution, as well as HRTEM-validated morphological changes, powerfully substantiates that Mn doping successfully tunes the optical behaviour of ZnO through induced controlled structural disorder and quantum confinement effects.

3.1.4 *Fourier Transform Infrared (FTIR) Spectroscopy*

A helpful method for identifying functional groups and chemical interactions in materials is FTIR spectroscopy (Aadnan et al., 2022; Dhivya et al., 2022). In this research, FTIR spectra of Mn-doped ZnO samples with different Mn concentrations (x = 0.02, 0.04, 0.06, 0.08, 0.1) were investigated to determine the structural and chemical changes induced by the incorporation of Mn (Fig. 4). The recorded peaks are rich in information on the nature of bonding, functional group presence, and potential impurities in the prepared materials (Aadnan et al., 2022; Fatolahi & Janani, 2024; Kanwal et al., 2023; Kumar et al., 2016; Silambarasan et al., 2024). The wide absorption peak in the low wavenumber region, that is, less than 600 cm^{-1} is one of the noteworthy characteristics observed in the FTIR spectra. This is associated with the Zn–O stretching vibrations, which confirms the formation of ZnO (Aadnan et al., 2022; Iqbal et al., 2024; Kanwal et al., 2023; Kistan et al., 2024; Kumar et al., 2016; Shatnawi et al., 2016; Silambarasan et al., 2024). Mn doping should introduce structural distortions, which may cause shifts to this characteristic Zn–O peak. These variations confirm successful Zn substitution by Mn in the ZnO lattice, which changes the vibrational modes of the material (Aadnan et al., 2022; Kanwal et al., 2023; Kistan et al., 2024; Shatnawi et al., 2016). A peak at 1197.72 cm^{-1} is due to bending vibrations of hydroxyl (-OH) groups. This indicates the existence of adsorbed water molecules or surface hydroxyl groups, which are usually present in ZnO materials (Kumar et al., 2016). The hydroxyl groups are responsible for the photocatalyst and antibacterial activities of ZnO since they are capable of being involved in reactive oxygen species (ROS) production upon light exposure.

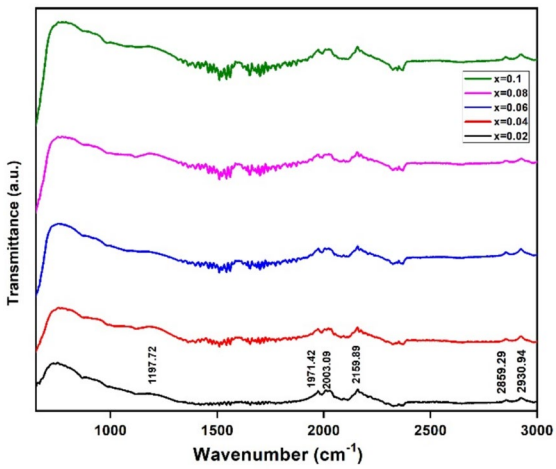

Fig. 4 FTIR of ZnO with Mn Doping [$Zn_{(1-x)}Mn_xO$, where x = 0.02, 0.04, 0.06, 0.08, 0.1]

Several peaks in the mid-infrared range, at 1971.42 cm^{-1}, 2003.09 cm^{-1}, and 2159.89 cm^{-1}, indicate the existence of carbonate species or residues of the organic precursors from the synthesis reaction. These peaks could be caused by CO_2 adsorption on the ZnO surface or by unreacted organic precursors. The detection of these peaks indicates the importance of optimizing the synthesis and annealing conditions to reduce such residues (Iqbal et al., 2024; Kanwal et al., 2023; Kistan et al., 2024; Kumar et al., 2016). Peaks in the region of the higher wavenumber are observed at 2859.29 cm^{-1} and 2930.94 cm^{-1}, representing C-H stretching vibrations (Kanwal et al., 2023; Silambarasan et al., 2024). The absence of distinct Mn–O peaks suggests that Mn is well integrated into the lattice of ZnO and is not separated into separate Mn-based oxides. These findings correlate with earlier structural analyses like X-ray diffraction (XRD), where peak broadening and shifts further confirm Mn substitution in the ZnO matrix.

3.1.5 *X-Ray Photoelectron Spectroscopy (XPS)*

XPS is a fundamental tool to find out the electronic structure and chemical makeup of materials (Iqbal et al., 2024; Kadam et al., 2021). The given XPS spectra represent the binding energy variations in ZnO with Mn doping (2%, 6%, and 10%). Zn 2p, O 1 s, and Mn 2p peak analyses assist us in comprehending the interaction of Mn with ZnO and the contribution of oxygen vacancies in modulating its properties (Iqbal et al., 2024; Kadam et al., 2021).

The Zn 2p spectra (Fig. 5a) of pure ZnO exhibit the typical Zn $2p_{3/2}$ and Zn $2p_{1/2}$ peaks at 1023.47 eV and 1046.12 eV, respectively, with a spin–orbit splitting of 22.65 eV. These are consistent with earlier reports on ZnO, which indicate the existence of Zn^{2+} in the wurtzite lattice structure (Aadnan et al., 2022; Achouri et al., 2016; Das et al., 2023; Iqbal et al., 2024; Kadam et al., 2021; Nithya et al., 2020; Shatnawi et al., 2016). Under 2% Mn doping

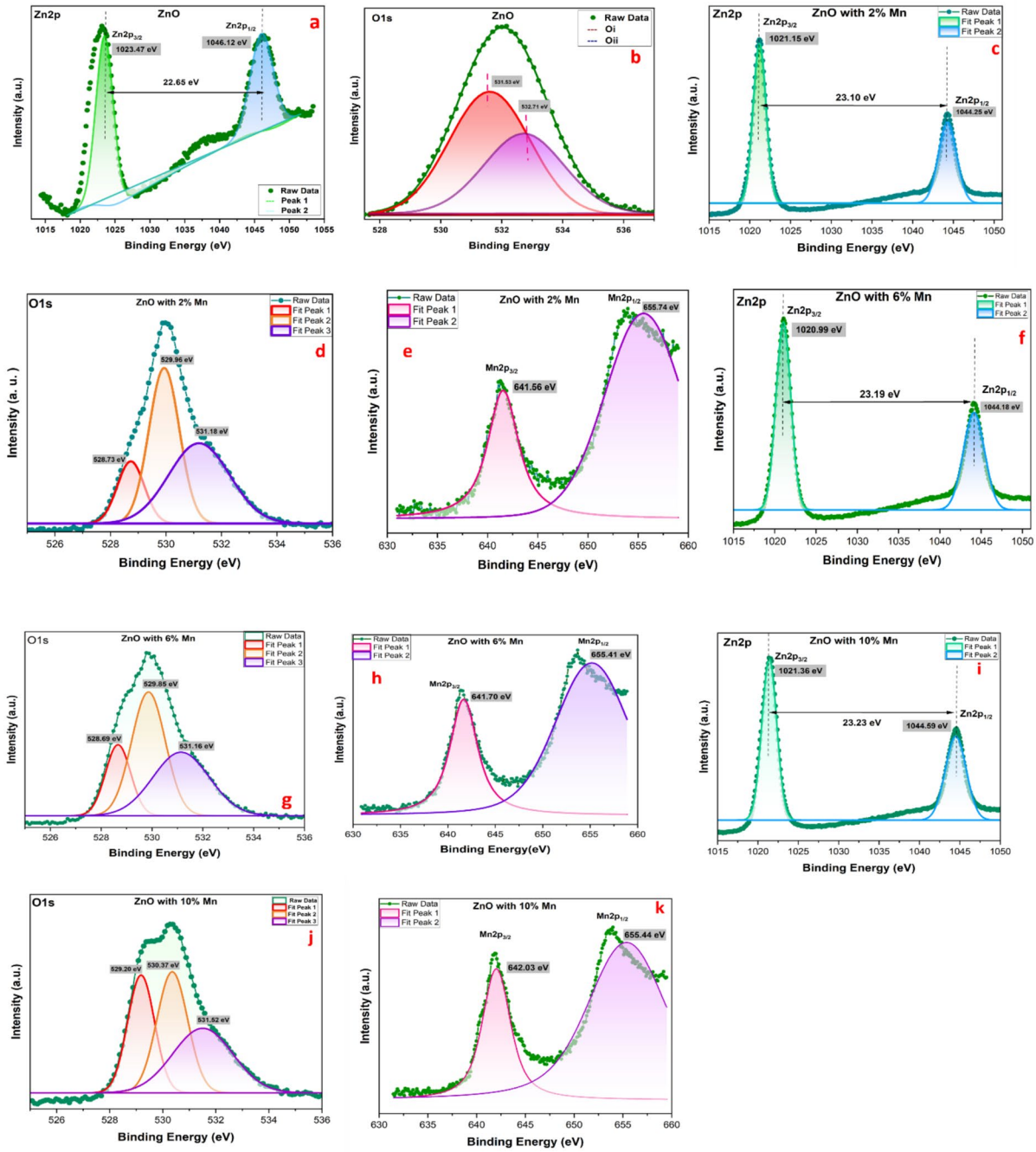

Fig. 5 **A a**: XPS spectra of Zn2p for pure ZnO **b**: XPS spectra of O1s for pure ZnO **c**: XPS spectra of Zn2p for 2% Mn doping **d**: XPS spectra of O1s for 2% Mn doping **e**: XPS spectra of Mn 2p for 2% Mn doping **f**: XPS spectra of Zn2p for 6% Mn doping **g**: XPS spectra of O1s for for 6% Mn doping **h**: XPS spectra of Mn 2p for 6% Mn doping **i**: XPS spectra of Zn2p for 10% Mn doping **j**: XPS spectra of O1s for 10% Mn doping **k**: XPS spectra of Mn 2p for 10% Mn doping

(Fig. 5c), one sees a little movement in the Zn $2p_{3/2}$ peak toward 1021.15 eV and that of the Zn $2p_{1/2}$ to 1044.25 eV with a further increment in spin–orbit splitting up to 23.10 eV. It means an environment change at the electronic level, due to substitution of ZnO with Mn^{2+} ions (Das et al., 2023; Shatnawi et al., 2016). For 6% Mn doping (Fig. 5f), the Zn $2p_{3/2}$ peak also shifts to 1020.99 eV, with Zn $2p_{1/2}$ at 1044.18 eV, with the splitting remaining at 23.19 eV. Likewise, for 10% Mn doping (Fig. 5i), the Zn $2p_{3/2}$ peak is at 1021.36 eV, and Zn $2p_{1/2}$ shifts to 1044.59 eV with a spin–orbit splitting of 23.23 eV. The downward shift of the binding energy with the rise in Mn doping reflects a redistribution of charge and formation of Mn–O-Zn bonds, thereby affecting the local electronic structure. The O 1 s spectrum (Fig. 5b) of pure ZnO shows two peaks at 531.53 eV and 532.71 eV for lattice oxygen (O^{2-}) and oxygen vacancies or surface hydroxyl groups, respectively (Aadnan et al., 2022; A. Das et al., 2023; Nithya et al., 2020). After 2% Mn doping (Fig. 5d), three peaks are observed at 528.73 eV, 529.96 eV, and 531.18 eV. The peak at 528.73 eV is due to Zn–O bonding, whereas the peaks at 529.96 eV and 531.18 eV represent oxygen vacancies and chemisorbed species (Aadnan et al., 2022; Das et al., 2023; Nithya et al., 2020). The enhancement of oxygen vacancy peak intensity indicates that Mn doping increases defect states in ZnO. For 6% Mn doping (Fig. 5g), the peaks are at 528.69 eV, 529.85 eV, and 531.16 eV and have a pattern similar to that of 2% doping with an increased contribution from oxygen vacancy. When 10% Mn doping (Fig. 5j) is done, the peaks go down to 529.20 eV, 530.37 eV, and 531.52 eV. The progressive rise in oxygen vacancies with Mn concentration shows the formation of mid-gap states, which may affect photocatalytic activity (Aadnan et al., 2022; Das et al., 2023). The ZnO lattice's assimilation of Mn is confirmed by the Mn 2p spectra. For 2% Mn doping (Fig. 5e), the Mn $2p_{3/2}$ and Mn $2p_{1/2}$ peaks are found at 641.56 eV and 655.74 eV, respectively. These values are typical for Mn^{2+}, meaning that Mn is replacing Zn sites (Aadnan et al., 2022; Achouri et al., 2016; Das et al., 2023; Iqbal et al., 2024; Kadam et al., 2021; Nithya et al., 2020; Shatnawi et al., 2016). For 6% Mn doping (Fig. 5h), the Mn $2p_{3/2}$ peak shifts to 641.70 eV, and the Mn $2p_{1/2}$ peak shifts to 655.41 eV. For 10% Mn doping (Fig. 5k), the peaks are at 642.03 eV and 655.44 eV, respectively. The small variation of Mn 2p peaks with increasing doping concentration indicates that Mn stays in the +2 oxidation state without experiencing notable electronic reconstruction. All of these XPS findings are consistent with earlier research on Mn-doped ZnO, where Mn incorporation generates oxygen vacancies and changes the local electronic structure. Zn 2p peak shift and oxygen vacancy-related O 1 s peak increase indicate that Mn doping creates defect states, potentially increasing photocatalytic activity by capturing charge carriers and lowering recombination rates. Furthermore, the Mn^{2+} presence without notable oxidation state change verifies that Mn primarily substitutes for Zn in the lattice instead of precipitating second phases.

3.1.6 Photocatalytic Degradation Efficiency of Mn-doped ZnO

Photocatalysis by ZnO is widely investigated for environmental cleanup, especially for the degradation of organic contaminants like dyes. Pure ZnO tends to suffer from high electron–hole recombination, making it less effective. To overcome this, transition metal doping with metals like Mn is used to alter its electronic property and make it more photocatalytic (Fatolahi & Janani, 2024). This study investigated the photocatalytic destruction of crystal violet beneath light irradiation using ZnO and Mn-doped ZnO (2%, 6%, and 10%). The degradation efficiencies obtained were 68.16% for pure ZnO, 72.55% for ZnO-2% Mn, 96.10% for ZnO-6% Mn, and 78.15% for ZnO-10% Mn. These differences in degradation efficiency can be attributed to changes in charge carrier dynamics, oxygen vacancy concentration, and structural changes due to Mn incorporation (Aadnan et al., 2022; Das et al., 2023; Silambarasan et al., 2024).

For the pure ZnO, the degradation efficiency was 68.16% within 140 min, as observed in Fig. 6(a). The continuous decline in absorbance with increasing time validates the photocatalytic effect. The photocatalytic activity in ZnO is initiated whenever an electron (e-) moves from the valence band (VB) to the conduction band (CB) by light energy equal to or greater than the bandgap, generating a hole (h+) in the VB. After then, these charge carriers take part in redox processes. Whereas hydroxyl radicals are produced when holes oxidize water, superoxide radicals are produced when photogenerated electrons reduce oxygen molecules. Both $O_2^{-}\bullet$ and OH• are highly

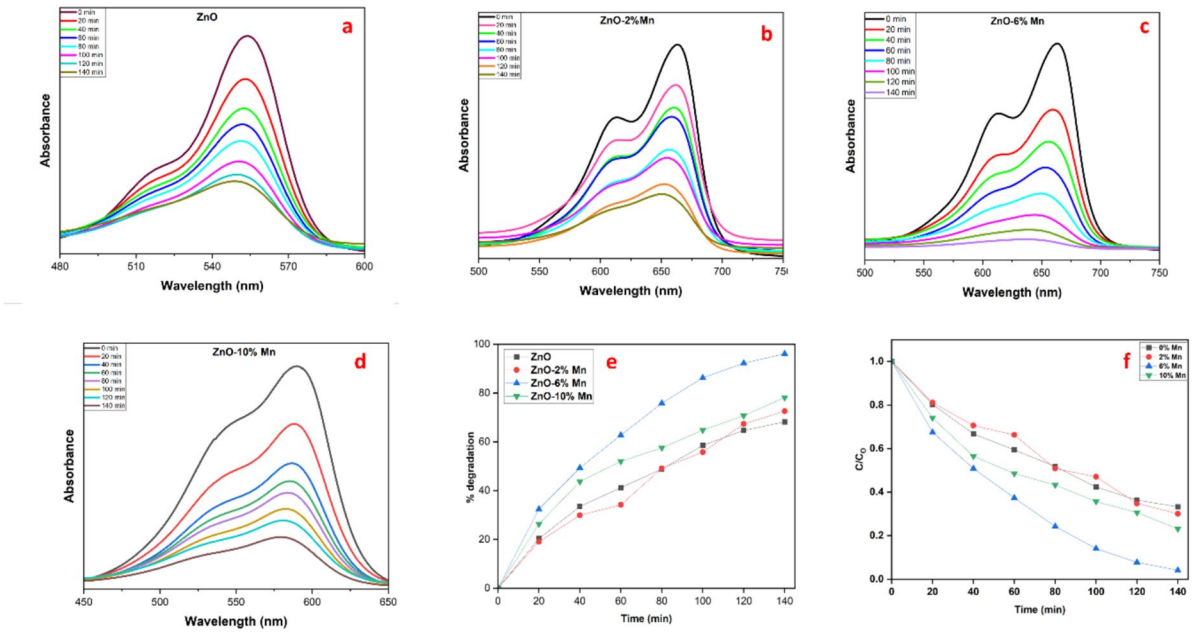

Fig. 6 **a**: Crystal Violet dye photocatalytic degradation employing ZnO as a photocatalyst **b**: Crystal Violet dye photocatalytic degradation employing ZnO with 2% Mn doping as a photocatalyst **c**: Crystal Violet dye photocatalytic degradation employing ZnO with 6% Mn doping as a photocatalyst **d**: Crystal Violet dye photocatalytic degradation employing ZnO with 10% Mn doping as a photocatalyst **e**: percentage of degradation versus time curves of Crystal Violet with $Zn_{(1-x)}Mn_xO$ [x = 0.00, 0.02, 0.06, 0.1] nanoparticles **f**: C/C_o versus time curves of Crystal Violet with $Zn_{(1-x)}Mn_xO$ [x = 0.00, 0.02, 0.06, 0.1] nanoparticles

reactive species that attack and break down the dye molecules into smaller, less toxic compounds. However, the efficacy of this mechanism is limited in pure ZnO due to the fast recombination of e-/h + couples (Aadnan et al., 2022; Das et al., 2023; Fatolahi & Janani, 2024).

After doping ZnO with 2% Mn, a small increment in degradation efficiency (72.55%) is noticed (Fig. 6b). This is due to Mn^{2+} serving as an electron trap, lowering the recombination rate and increasing charge carrier lifetime. Moreover, the addition of Mn introduces more oxygen vacancies, as earlier proven by XPS experiments, which improve charge separation and ensure greater photocatalytic activity (Das et al., 2023; Kistan et al., 2024). Nevertheless, the improvement is quite modest, suggesting that 2% Mn doping is not enough to induce a dramatic shift in catalytic activity.

The most notable improvement is seen for ZnO-6% Mn, with the degradation efficiency being 96.10% (Fig. 6c). This marked improvement can be explained by some important factors. First, the addition of Mn^{2+} at an optimum concentration increases oxygen vacancy density by a considerable extent, as seen from O 1 s XPS spectra. These vacancies are sites for charge separation, avoiding electron–hole recombination and promoting photocatalytic efficiency. Second, Mn doping minimally alters the band structure of ZnO, which can reduce the band gap, thus enhancing the absorption of light and producing more charge carriers after being exposed to light. The Mn also affects the formation of reactive species, resulting in an increased number of hydroxyl radicals and superoxide radicals that efficiently break down crystal violet molecules to CO_2 and H_2O. Das et al. (2023) show similar results, where the best results were shown by 1% Mn doping, then 3% and 5% Mn doping when tested with Congo red under visible light (Das et al., 2023). Achouri et al. (2016) show the best results with 3% Mn doping rather than 5% and 7% when tested for Orange (II) dye under solar light irradiation (Achouri et al., 2016). Daphne Mary John et al. tested the degradation of sulfamethazine in the presence of direct sunlight, where degradation of ZnO was better

compared to 2% and 5% Mn-doped ZnO (Fatolahi & Janani, 2024).

At 10% Mn doping, the efficiency of degradation drops to 78.15% (Fig. 6d). Even with the presence of extra Mn, over-doping creates recombination centres instead of enhancing charge separation. This is because excessive Mn can cause lattice distortion and defects that trap electrons and holes, thus lowering the efficiency of charge carrier migration (Achouri et al., 2016; Silambarasan et al., 2024). Also, earlier XPS research indicated that at elevated Mn concentrations, secondary phases like MnO_x may be formed, which do not play an important role in photocatalysis. Therefore, the degradation efficiency is lower than that of ZnO-6%Mn but still greater than that of pure ZnO owing to the presence of some useful Mn-induced modifications.

The trends of degradation in Fig. 6e further validate the effect of Mn doping. Kinetic analysis indicates that ZnO-6%Mn degrades crystal violet at the highest rate, followed by pure ZnO and ZnO-2%Mn with slower degradation. ZnO-10%Mn initially indicates a better rate but decreases with time due to enhanced recombination. The trends observed are in good agreement with the previously achieved XPS and structural data. The Zn 2p and Mn 2p spectra verified successful incorporation of Mn, whereas the O 1 s spectra indicated increased density of oxygen vacancies with Mn doping up to 6%. Beyond this concentration, the vacancy density might not further increase, resulting in the noted reduction in efficiency at 10% doping. A previous study by Du et al., in Du et al., 2025, shows successful photocatalytic degradation of Hg^0 using novel Bi_2O_2S/Bi_5O_7I/ZA hydrogel photocatalyst and achieved a removal efficiency of 95% (Du et al., 2025). Further, Han et al. used boron-doped nanodiamond/TiO_2/MXene photocatalyst for tetracycline degradation (Han et al., 2025). Both mentioned studies support the findings of this study.

The C/C_o vs. time plot is a precise quantitative representation of crystal violet photocatalytic degradation kinetics under various doping conditions (Fig. 6e). The initial concentration (C_o) is the absorbance of the dye solution at $t=0$, and its progressive reduction over time ($C/C_o<1$) indicates the progressive degradation of the dye molecules. The slope of the decreasing rate of C/C_o is a key indicator of photocatalytic performance, since the greater the slope, the more rapid the degradation and the greater the catalytic activity (Akram et al., 2023; Dhivya et al., 2022; Kistan et al., 2024; Nithya et al., 2020).

Among the tested samples, ZnO-6% Mn has the steepest decrease in C/C_o, which further proves its best photocatalytic activity. The steep drop implies that this sample produces a larger amount of "hydroxyl radicals (OH•)", "reactive oxygen species (ROS)", and superoxide radicals (O_2^{-}•), which could effectively break the crystal violet molecules. The improved performance is due to the optimized level of Mn doping, which brings about favourable structural changes, such as enhanced oxygen vacancies and better charge separation. These together result in decreased electron–hole recombination and enhanced photocatalytic activity (Das et al., 2023; Silambarasan et al., 2024).

The trends observed in the C/C_o vs. time plot are consistent with the trends in degradation efficiency shown in Fig. 6(e). ZnO-6% Mn always shows the highest efficiency (96.10% degradation), while lower doping concentrations (2%) and over-doping (10%) show lower performance due to varying charge carrier recombination dynamics. These results indicate the importance of the doping concentration in photocatalysis and stress that 6% Mn doping is the most favourable percentage for maximum efficiency in crystal violet degradation.

Mn doping significantly affects ZnO's photocatalytic efficiency, and the highest degradation efficiency of 96.10% is achieved by 6% doping concentration. The improvement is mainly attributed to enhanced charge separation, increased oxygen vacancy, and minor bandgap alteration. Lower Mn doping (2%) gives limited improvement, while over-doping (10%) lowers efficiency through charge recombination and potential secondary phase development. These results highlight the need to optimize doping levels for the highest photocatalytic activity. Future research might involve co-doping protocols or surface treatment to further optimize the stability and efficiency of Mn-doped ZnO photocatalysts for practical wastewater treatment processes.

3.2 Performance Evaluation of the MFCs

3.2.1 Polarization Studies of the MFCs

From the above results, the 6% Mn-doped ZnO shows the best results among all the concentrations. Hence,

it was applied to the cathode electrode at a concentration of 1, 1.5, 2, and 2.5 mg/cm^2. The synthesized Mn-doped ZnO has been used in MFC as a cathode catalyst, and its performance has been evaluated. Polarization experiments on the cathode catalyst in MFCs are performed to assess the electrochemical performance of the catalyst and its proficiency in reducing oxygen. This experiment determines the overpotential, activation losses, and overall impact on the power generation of the catalyst. Based on the analysis of polarization curves, the catalyst concentration could be optimized to increase efficiency in MFCs. To date, a lot of research has been done on using ZnO as a cathode catalyst. Other researchers used ZnO as a cathode catalyst in MFCs and were able to reach a maximum power density of 90.177 mW/m^3 (El-Khatib et al., 2023). Hence, in this study, Mn-doped ZnO was used at various concentrations. Figure 7a shows the full cell study of all the MFCs. The half-cell cathode study is given in Fig. 7b. With 2.00 mg/cm^2 Mn-ZnO, the highest volumetric power density of 12.51 W/m^3 was attained. The power density increased several times in comparison with studies with a ZnO cathode catalyst. The volumetric power density of the MFC with an unmodified anode is 8.90 W/m^3. The power density of the MFC gradually increases with increasing catalyst concentration. In the year 2025, Zhao et al., successfully improved the Stacked MFC performance using capacitive-hydrogel bioanodes and achieved around 1.87% increase in power density of the MFCs (Zhao et al., 2025). Also, Zhu et al., in Zhu et al., 2025, optimized a few parameters using response surface methodology and improved the power density and treatment of sewage in a fluidized MFC (Zhu et al., 2025).

The Mn-ZnO cathode catalyst increases the power density of MFCs in this study because of its superior electrocatalytic activity and enhanced oxygen reduction reaction (ORR) kinetics. The Mn-ZnO cathode catalyst's surface chemistry includes the production of ROS from ZnO and Mn, which have antimicrobial properties to inhibit biofouling. The ZnO component also has a slightly hydrophilic character, inhibiting organic deposition and microbial adhesion, thus ensuring catalytic efficiency in MFCs. The enhanced power density at 2.00 mg/cm^2 is due to the synergy of electronic interactions among Mn and Zn in the ZnO lattice. Lattice strain and oxygen vacancies, which result from Mn doping, enhance oxygen molecule adsorption and electron transfer kinetics. These modifications likely shift the conduction band and increase charge carrier density on the cathode surface, which is necessary for the ORR. The structural optimisation, coupled with ideal catalyst loading, increases MFC performance beyond previously reported ZnO-based studies, demonstrating the novelty and functional superiority of the nanocomposite (Kerli et al., 2014). As observed in Fig. 7a, beyond a certain threshold concentration, the power density decreases slightly because of catalyst agglomeration, which means that less active surface area is available for the oxygen reduction reaction (ORR). Excess

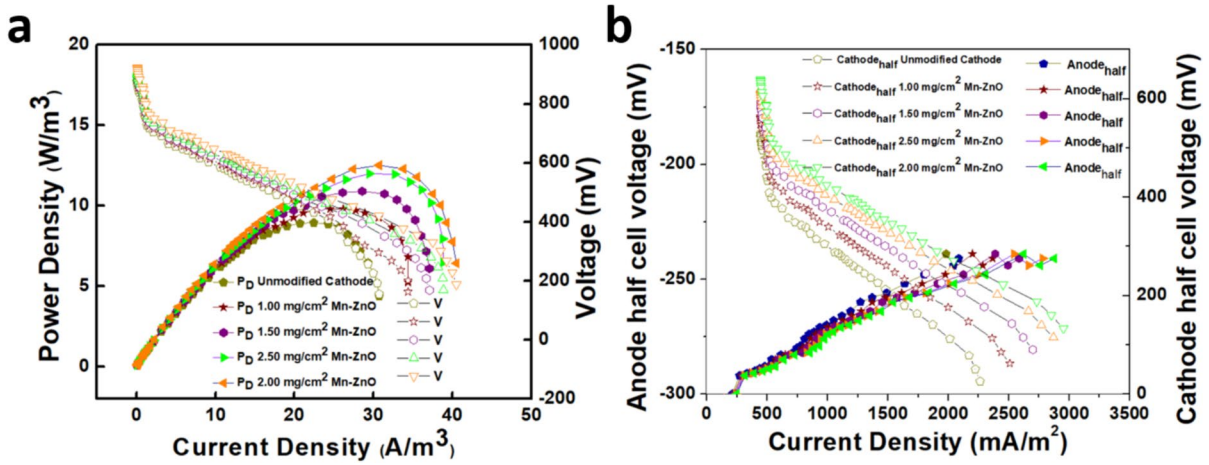

Fig. 7 Polarization Study **a** Full Cell Polarization Study **b** Half Cell Study

catalyst can also enhance internal resistance and impede electron transfer, resulting in increased overpotentials. Moreover, an excess loading of the catalyst may clog mass transport channels, restricting oxygen diffusion towards the sites of reaction (Dange et al., 2022; Nabil et al., 2022; Savla et al., 2020).

3.2.2 *Linear Sweep Voltammetry (LSV), and Electrochemical Impedance Studies (EIS) of the MFCs*

The charge transfer characteristics of electroactive components are evaluated using electrochemical impedance spectroscopy, or EIS. The relevant electrochemical properties of the electrode (imaginary component vs. real component of impedance) are examined using a Nyquist plot. Each point makes a unique semicircle in the highest frequency range and a straight line in the lowest frequency band. Each electrode's Charge Transfer Resistance (Rct) is calculated using the semicircles'diameter. There is a noticeable fluctuation in the semicircular region of the anode's impedance curve (Fig. 8b).

The Rct values of the MFCs display the following hierarchy: Mn-doped ZnO cathode without alteration (286 Ω) > 1.00 mg/cm^2 (208.60 Ω) > 1.50 mg/cm^2 (170.60 Ω) > 2.50 mg/cm^2 (98.92 Ω) > 2.00 mg/cm^2 (90.90 Ω). A low "Rct" and higher "power output" were the results of the enhanced Mn-doped ZnO loading rate, which, up to a certain threshold, produced a large number of active sites for ORR activity. Because of the reduced Rct, the ORR overpotential for Mn-doped ZnO falls. The findings are consistent with the study on polarization. Furthermore, Mn-doped ZnO exhibits increased electrochemical activity due to the efficient transmission of electrons to the component where the oxygen reduction occurs. The significant decrease in Rct with increased catalyst loading indicates an improved electron transfer rate at the cathode interface. Mn doping in the ZnO matrix changes its electronic structure, probably reducing the bandgap and improving faster electron mobility, hence lowering the kinetic barrier for the ORR (Kistan et al., 2024).

Now, to compare the Mn-doped ZnO catalyst with a commercially available platinum (Pt) catalyst, linear sweep voltammetry (LSV) was done. One of the electrochemical techniques used to investigate the ORR's mechanism is LSV. Based on the results of the polarization study and EIS, a 2.00 mg/cm^2 concentration was chosen for this study. The electrochemical performance of an unmodified cathode, a "cathode" loaded with 2.00 mg/cm^2 zinc stannate, and a "cathode" loaded with 2.00 mg/cm^2 Pt/C is contrasted in the LSV graph (Fig. 8b). The results of the synthesized cathode catalyst were compared to the expensive Pt/C catalyst. The current response is measured using

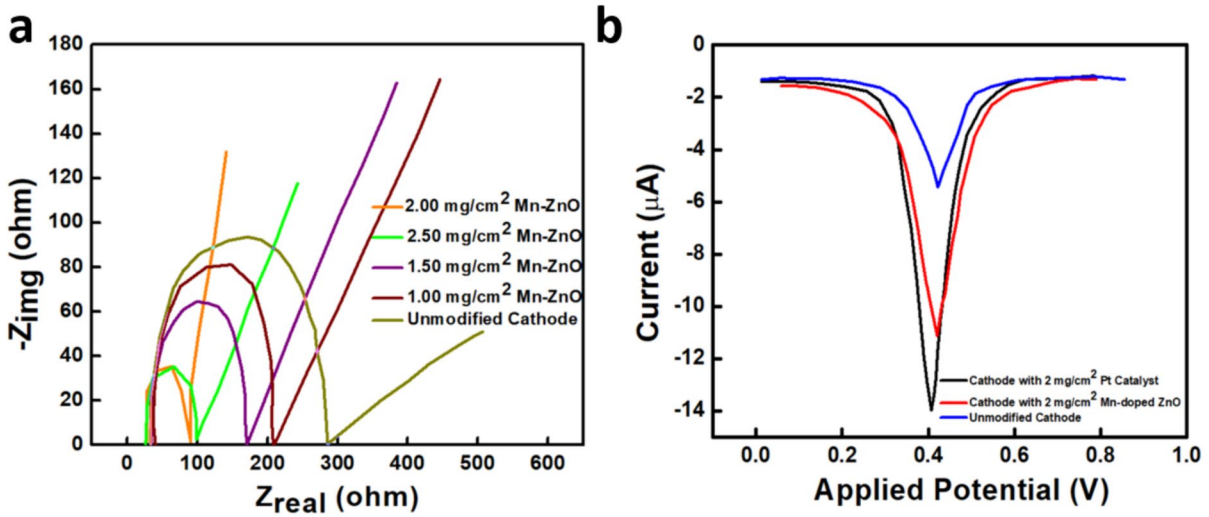

Fig. 8 **a** EIS Study of MFCs with various Catalyst Concentrations **b** LSV Study of MFC with Mn-ZnO and MFC with Pt-Loaded Cathode

the applied potential in order to evaluate the ORR activity.

The unmodified cathode shows no reduction peak. Due to the metal oxide composition and spinel structure, the cathode containing Mn-doped ZnO shows a noticeable peak at 0.4 V, which enhances ORR activity. This improvement would suggest that Mn-doped ZnO functions as a cathode catalyst for oxygen reduction and electron acceptance. Because of platinum's proven catalytic effectiveness for the ORR, the cathode loaded with Pt/C showed the most significant current and a more noticeable peak, as was to be expected. However, the Mn-doped ZnO loaded cathode was notable due to its cost-effectiveness and environmental friendliness, even if its performance was somewhat poorer than that of Pt/C. Therefore, in MFCs, Mn-doped ZnO can be an excellent catalyst in the place of expensive Pt/C.

3.2.3 Biofouling Study on Cathode Electrode Surface

Confocal Laser Scanning Microscopy (CLSM) is employed for investigating biofouling on the cathode surface through the presentation of high-resolution, 3D imaging of microbial adhesion and biofilm growth. The examination is essential in the assessment of the antifouling property of Mn-doped ZnO. The cathode electrode with no Mn-doped ZnO shows the maximum biofouling. The biofouling reduces with the addition of Mn-doped ZnO as a cathode catalyst. As seen in Fig. 9, the decrease happens as the amount of Mn-doped ZnO rises. After a certain threshold, no observable change was observed in the biovolume of cell biomass. Biofilm biovolume and surface coverage were quantified from CLSM images using COMSTAT software, analyzing at least five random fields per sample to provide statistically significant results (Fig. 9f). The results mimic those from the polarization, LSV, and EIS study. The antifouling property of Mn-doped ZnO can be mechanistically ascribed to its capability to produce reactive oxygen species (ROS) like hydroxyl radicals and superoxides at ambient and cathodic conditions that suppress microbial growth. The weak hydrophilicity of ZnO also hinders the attachment of organic macromolecules, thus suppressing the formation of biofilms. As observed in CLSM images, the biovolume of attached cells reduced steadily with rising catalyst loading, confirming the bio-inhibitory surface properties of the material. Such properties are especially valuable for extended MFC operation, providing a dual-purpose cathode surface that facilitates electrochemical activity while ensuring biofouling resistance (Iqbal et al., 2024).

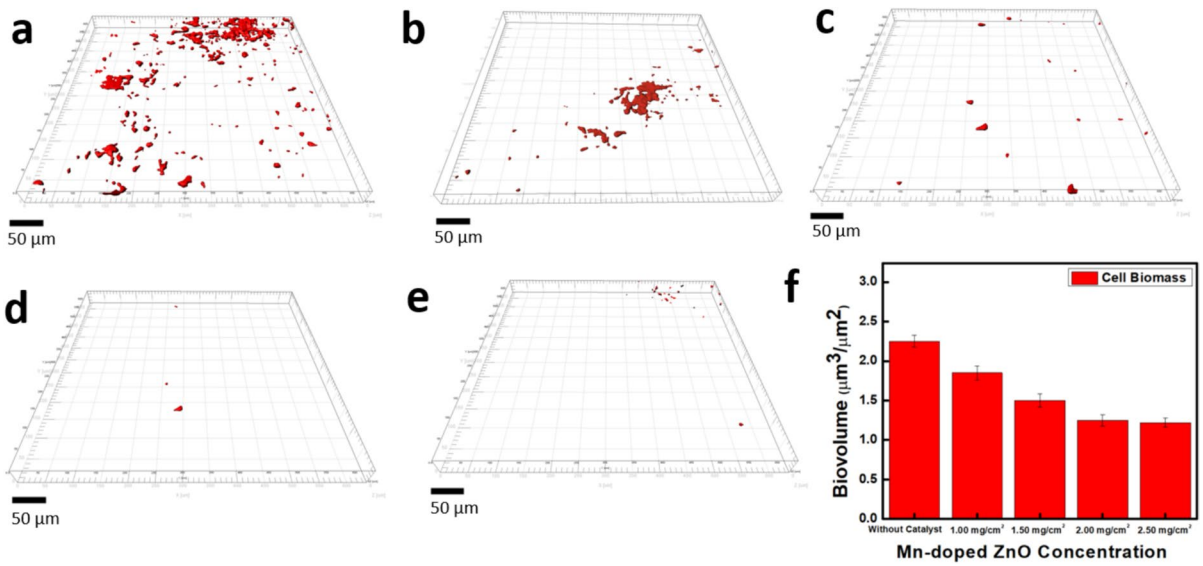

Fig. 9 CSLM Studies of Biofouling upon the cathode electrode. **a** Without a cathode catalyst **b** 1.00 mg/cm^2 Mn-doped ZnO **c** 1.50 mg/cm^2 Mn-doped ZnO **d** 2.00 mg/cm^2 Mn-doped ZnO **e** 2.50 mg/cm^2 Mn-doped ZnO **f** Biovolume of Cell Biomass

Table 1 Previous similar studies in bioelectrochemical systems

S. No	Cathode Catalyst and Bioelectrochemical System	Obtained Power Density	Reference
1	Bismuth-doped TiO_2 (in MFC)	244 mW/m^2	(Bhowmick et al., 2018)
2	$CoFe_2O_4$ doped TiO_2 (in Microbial Desalination Cell)	4.56 W/m^3	(Sahni et al., 2024)
3	Lithium-doped Bismuth Ferrite (in MFC)	8.2 W/m^3	(Pema et al., 2023)
4	ZnO (in MFC)	90.177 mW/m^3	(El-Khatib et al., 2023)
5	Manganese-doped ZnO in MFC	12.15/m^3	This Study

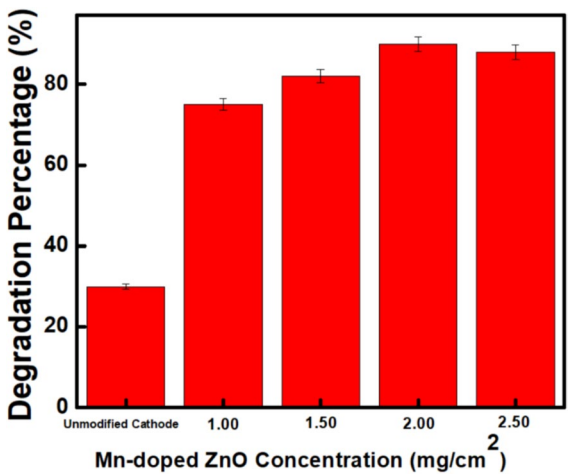

Fig. 10 Crystal Violet Dye Degradation at Various Concentrations of Cathode Catalyst in MFC

Few similar studies that used a catalyst on the cathode electrode to enhance MFC performance are given in Table 1.

3.2.4 Photocatalytic Degradation of Crystal Violet in MFC

In Section 3.1.6, various concentrations of Mn were tested for photocatalytic degradation in conical flasks, and 6% Mn-doped ZnO was selected as the cathode catalyst for further evaluation in MFCs. This section assesses the photocatalytic degradation performance within MFCs. The study was conducted using a UV spectrophotometer (Kadam et al., 2021), following the same procedure as described in Section 3.1.6. With a catalyst loading of 2 mg/cm^2, the MFC achieved a maximum degradation efficiency of approximately 95% (Fig. 10), closely matching the 96.10% efficiency observed in conical flasks. However, at a loading of 2.5 mg/cm^2, the degradation efficiency slightly declined. Mn doping improves the photocatalytic activity of ZnO by introducing intermediate energy levels in the bandgap that facilitate electron excitation under UV and potentially visible light. Photogenerated electrons reduce oxygen to produce superoxide radicals, while holes oxidize water to give hydroxyl radicals, which are responsible for the fragmentation of crystal violet dye molecules. The similar degradation efficacy in MFC and flask experiments is an indicator of resilient catalytic activity even under operational electrochemical conditions. This two-fold capability — effective electron uptake for ORR and photocatalytic destruction of dye — makes Mn-ZnO a multifaceted catalyst, more superior than conventional single-point cathode materials in wastewater-integrated bioelectrochemical systems. These results confirm that the catalyst exhibits photocatalytic activity in the MFC while also enhancing the oxygen reduction reaction (ORR) (Akram et al., 2023).

4 Conclusion

The successful doping of ZnO nanoparticles with Mn was established through a range of characterization methods, proving the structural, optical, and morphological changes caused by Mn doping. XRD confirmed the preservation of the wurtzite ZnO phase with minor lattice deformations upon Mn doping. UV–Vis revealed narrowing of the bandgap, which improves visible light absorption, while FTIR and XPS established the incorporation of Mn in the ZnO lattice with an increase in oxygen vacancies. HRTEM imaging indicated that the nanoparticles were well-dispersed with less agglomeration, justifying the contribution of Mn in altering ZnO's structural character. The synthesized Mn-doped ZnO was used as a cathode catalyst in MFC for enhanced ORR

and simultaneous photocatalytic degradation of dye. Photocatalytic crystal violet degradation indicated that Mn doping had a great impact on photocatalytic efficiency, where 6% Mn doping exhibited the highest degradation (96.10%) due to maximum charge carrier separation and increased generation of reactive species. Yet, high Mn content (10%) reduced efficiency owing to the creation of recombination centers. These findings highlight the significance of maximization of Mn doping levels towards attaining the best photocatalytic performance. Further, in MFC, the 6% Mn-doped ZnO showed a maximum power density of 12.51 W/m^3. The synthesized catalysts were compared with a commercially available Pt catalyst, and the results confirmed that Mn-doped ZnO can be a good alternative to the expensive Pt catalyst. Future studies include the connection of MFCs in a stack to increase the output. A proper harvesting of the energy generated can also be a part of future studies. Therefore, this study contributes valuable information on the environmentally friendly synthesis of efficient Mn-doped ZnO-based photocatalysts and their subsequent application in MFC for improved ORR and concurrent dye degradation.

Authors Contributions SC and SP: Conceptualization, Data Collection, Writing, Reviewing, and Editing; AG and MS: Data Collection, Writing, Reviewing, and Editing; MR and HSG: Writing, Reviewing, and Editing; EFK: Writing, Reviewing, Supervision, and Editing.

Funding Open access funding provided by University of Johannesburg.

Data Availability The data supporting this study's findings are available on reasonable request from the corresponding author.

Declarations

Ethical Approval This work has been carried out under the auspices of the Sharda University and the Saveetha Institute of Medical and Technical Sciences (SIMATS) in India, as well as the University of Johannesburg in South Africa. All the authors agreed to participate in this work.

Consent for Publication All the authors agree to have this work published by the Journal of Water, Air & Soil Pollution.

Competing Interests The authors declare that they have no known competing financial interests or personal relationships that could have appeared to influence the work reported in this paper. No data was used for the research described in the article.

Open Access This article is licensed under a Creative Commons Attribution 4.0 International License, which permits use, sharing, adaptation, distribution and reproduction in any medium or format, as long as you give appropriate credit to the original author(s) and the source, provide a link to the Creative Commons licence, and indicate if changes were made. The images or other third party material in this article are included in the article's Creative Commons licence, unless indicated otherwise in a credit line to the material. If material is not included in the article's Creative Commons licence and your intended use is not permitted by statutory regulation or exceeds the permitted use, you will need to obtain permission directly from the copyright holder. To view a copy of this licence, visit http://creativecommons.org/licenses/by/4.0/.

References

Aadnan, I., Zegaoui, O., El Mragui, A., Daou, I., Moussout, H., & Silva, J. C. G. (2022). Structural, optical and photocatalytic properties of Mn doped ZnO nanoparticles used as photocatalysts for azo-dye degradation under visible light. *Catalysts, 12*, 1382. https://doi.org/10.3390/catal12111382

Achouri, F., Corbel, S., Balan, L., Mozet, K., Girot, E., Medjahdi, G., Said, M. B., Ghrabi, A., & Schneider, R. (2016). Porous Mn-doped ZnO nanoparticles for enhanced solar and visible light photocatalysis. *Materials & Design, 101*, 309–316. https://doi.org/10.1016/j.matdes.2016.04.015

Ahmed, S. A. (2017). Structural, optical, and magnetic properties of Mn-doped ZnO samples. *Results in Physics, 7*, 604–610. https://doi.org/10.1016/j.rinp.2017.01.018

Akram, R., Fatima, A., Almohaimeed, Z. M., Farooq, Z., Qadir, K. W., & Zafar, Q. (2023). Photocatalytic degradation of methyl green dye mediated by pure and Mn-doped zinc oxide nanoparticles under solar light irradiation. *Adsorption Science & Technology, 2023*, 5069872. https://doi.org/10.1155/2023/5069872

Arefi, M. R., & Rezaei-Zarchi, S. (2012). Synthesis of zinc oxide nanoparticles and their effect on the compressive strength and setting time of self-compacted concrete paste as cementitious composites. *International Journal of Molecular Sciences, 13*, 4340–4350. https://doi.org/10.3390/ijms13044340

Bezzeghoud, M., Ergüler, Z. A., Rodrigo-Comino, J., Jat, M. K., Kalatehjari, R., Bisht, D. S., Biswas, A., Chaminé, H. I., Shah, A. A., Radwan, A. E., Knight, J., Panagoulia, D., Kallel, A., Turan, V., Chenchouni, H., Ciner, A., & Gentilucci, M. (Eds.). (2024). *Recent Research on Geotechnical Engineering, Remote Sensing, Geophysics and Earthquake Seismology: Proceedings of the 2nd MedGU, Marrakesh 2022 (Volume 3)*. Springer Nature Switzerland. https://doi.org/10.1007/978-3-031-48715-6

Bhowmick, G. D., Noori, Md. T., Das, I., Neethu, B., Ghangrekar, M. M., & Mitra, A. (2018). Bismuth doped TiO2 as an excellent photocathode catalyst to enhance the performance of microbial fuel cell. *International Journal of Hydrogen Energy, 43*(15), 7501–7510. https://doi.org/10.1016/j.ijhydene.2018.02.188

Capellán-Pérez, I., Mediavilla, M., de Castro, C., Carpintero, Ó., & Miguel, L. J. (2014). Fossil fuel depletion and socio-economic scenarios: An integrated approach. *Energy, 77*, 641–666.

Chenchouni, H., Zhang, Z., Bisht, D. S., Gentilucci, M., Chen, M., Chaminé, H. I., Barbieri, M., Jat, M. K., Rodrigo-Comino, J., Panagoulia, D., Kallel, A., Biswas, A., Turan, V., Knight, J., Çiner, A., Candeias, C., & Ergüler, Z. A. (Eds.). (2024). *Recent Advancements from Aquifers to Skies in Hydrogeology, Geoecology, and Atmospheric Sciences: Proceedings of the 2nd MedGU, Marrakesh 2022 (Volume 1)*. Springer Nature Switzerland. https://doi.org/10.1007/978-3-031-47079-0

Cheng, C. Y., Liang, F. Y., & Chung, Y. C. (2014). Electricity generation from crystal violet using a single-chambered microbial fuel cell inoculated *Aeromonas hydrophila* YC 57. *Advanced Materials Research, 860*, 466–471.

Çiner, A., Barbieri, M., Khan, M. F., Ugulu, I., Turan, V., Knight, J., Rodrigo-Comino, J., Chenchouni, H., Radwan, A. E., Kallel, A., Panagoulia, D., Candeias, C., Biswas, A., Chaminé, H. I., Gentilucci, M., Bezzeghoud, M., & Ergüler, Z. A. (Eds.). (2024). *Recent Research on Environmental Earth Sciences, Geomorphology, Soil Science and Paleoenvironments: Proceedings of the 2nd MedGU, Marrakesh 2022 (Volume 4)*. Springer Nature Switzerland. https://doi.org/10.1007/978-3-031-48754-5

Corpuz, R. D., De Juan-Corpuz, L. M., & Kheawhom, S. (2021). Manganese Dioxide (MnO2): A High-Performance Energy Material for Electrochemical Energy Storage Applications. In S. Rajendran, J. Qin, F. Gracia, & E. Lichtfouse (Eds.), *Metal and Metal Oxides for Energy and Electronics* (Vol. 55, pp. 91–119). Springer International Publishing. https://doi.org/10.1007/978-3-030-53065-5_3

Dange, P., Savla, N., Pandit, S., Bobba, R., Jung, S. P., Gupta, P. K., Sahni, M., & Prasad, R. (2022). A comprehensive review on oxygen reduction reaction in microbial fuel cells. *Journal of Renewable Materials, 10*(3), 665.

Das, A., Liu, D., Wary, R. R., Vasenko, A. S., Prezhdo, O. V., & Nair, R. G. (2023). Mn-modified ZnO nanoflakes for optimal photoelectrochemical performance under visible light: Experimental design and theoretical rationalization. *The Journal of Physical Chemistry Letters, 14*, 9604–9611. https://doi.org/10.1021/acs.jpclett.3c02730

Degefa, A., Bekele, B., Jule, L. T., Fikadu, B., Ramaswamy, S., Dwarampudi, L. P., Nagaprasad, N., & Ramaswamy, K. (2021). Green synthesis, characterization of zinc oxide nanoparticles, and examination of properties for dye-sensitive solar cells using various vegetable extracts. *Journal of Nanomaterials*. https://doi.org/10.1155/2021/3941923

Dhivya, A., Rakhi, Y., & Stella Packiam, C. (2022). An eco-approach synthesis of undoped and Mn doped ZnO nano-photocatalyst for prompt decoloration of methylene blue dye. *Materials Today: Proceedings, 48*, 494–501. https://doi.org/10.1016/j.matpr.2021.02.751

Du, H., Zhang, A., Zhang, Q., Sun, Y., Zhu, H., Wang, H., Tan, Z., Zhang, X., & Chen, G. (2025). Fabrication of recoverable Bi_2O_2S/Bi_5O_7I/ZA hydrogel beads for enhanced photocatalytic Hg^0 removal in the presence of H_2O_2. *Separation and Purification Technology, 359*, Article 130597. https://doi.org/10.1016/j.seppur.2024.130597

El-Khatib, K., Khodary, D., Elzamik, F., Abdelbasit, H., & Moustafaa, G. (2023). Wastewater treatment and electricity generation via microbial fuel cell using ZnO supported on activated carbon cathode electrocatalyst. *Egyptian Journal of Chemistry, 0*(0), 0–0. https://doi.org/10.21608/ejchem.2023.199316.7716

Faisal, S., Jan, H., Shah, S. A., Shah, S., Khan, A., Akbar, M. T., Rizwan, M., Jan Wajidullah, F., Akhtar, N., Khattak, A., & Syed, S. (2021). Green Synthesis of Zinc Oxide (ZnO) Nanoparticles Using Aqueous Fruit Extracts of Myristica fragrans. *Their Characterizations and Biological and Environmental Applications, ACS Omega, 6*, 9709–9722. https://doi.org/10.1021/acsomega.1c00310

Fatolahi, L., & Janani, B. J. (2024). Rapidly chemical preparation of Mn doped ZnO nanostructures for photocatalysis efficiency based on UV light system and mechanism insights. *Physica Scripta, 99*, Article 065959. https://doi.org/10.1088/1402-4896/ad478e

Gadipelly, C., Pérez-González, A., Yadav, G. D., Ortiz, I., Ibáñez, R., Rathod, V. K., & Marathe, K. V. (2014). Pharmaceutical industry wastewater: Review of the technologies for water treatment and reuse. *Industrial & Engineering Chemistry Research, 53*, 11571–11592. https://doi.org/10.1021/ie501210j

Han, Q., Wang, L., Li, J., Dong, Y., Ma, Y., Zhang, J., & Yu, S. (2025). Built-in field-driven S-scheme boron-doped nanodiamond/TiO2(101)/MXene photocatalyst for efficient antibiotic elimination: Mechanisms and DFT validation. *Chemical Engineering Journal, 519*, Article 165290. https://doi.org/10.1016/j.cej.2025.165290

Iqbal, T., Afzal, M., Al- Asbahi, B. A., Afsheen, S., Maryam, I., Mushtaq, A., Kausar, S., & Ashraf, A. (2024). Enhancing apple shelf life: A comparative analysis of photocatalytic activity in pure and manganese-doped ZnO nanoparticles. *Materials Science in Semiconductor Processing, 173*, Article 108152. https://doi.org/10.1016/j.mssp.2024.108152

Jayachandran, A., Nair, A. T. R., & A.S. (2021). Green synthesis and characterization of zinc oxide nanoparticles using Cayratia pedata leaf extract. *Biochem. Biophys. Rep*, *26*, 100995. https://doi.org/10.1016/j.bbrep.2021.100995.

Kadam, S. A., Thomas, S. A., Ma, Y.-R., Maria Jose, L., Sajan, D., & Aravind, A. (2021). Investigation of adsorption and photocatalytic behavior of manganese doped zinc oxide nanostructures. *Inorganic Chemistry Communications, 134*, Article 108981. https://doi.org/10.1016/j.inoche.2021.108981

Kanwal, S., Tahir Khan, V., Tirth, V., Algahtani, A., Al-Mughanam, T., & Zaman, A. (2023). Room-temperature ferromagnetism in Mn-doped ZnO nanoparticles synthesized by the sol-gel method. *ACS Omega, 8*, 28749–28757. https://doi.org/10.1021/acsomega.3c03418

Karam, S. T., & Abdulrahman, A. F. (2022). Green synthesis and characterization of ZnO nanoparticles by using thyme plant leaf extract. *Photonics, 9*, 594. https://doi.org/10.3390/photonics9080594

Kebede Urge, S., Tiruneh Dibaba, S., & Belay Gemta, A. (2023). Green synthesis method of ZnO nanoparticles using extracts of *Zingiber officinale* and garlic bulb (*Allium sativum*) and their synergetic effect for

antibacterial activities. *Journal of Nanomaterials*. https://doi.org/10.1155/2023/7036247

Kerli, S., Alver, U., & Yaykaşlı, H. (2014). Investigation of the properties of In doped NiO films. *Applied Surface Science, 318*, 164–167. https://doi.org/10.1016/j.apsusc.2014.02.141

Kistan, A., Mohan, S., Mahalakshmi, S., Jayanthi, A., Ramya, A. J., & Karthik, P. S. (2024). Sol-gel technique, characterization and photocatalytic degradation activity of Manganese doped ZnO nanoparticles. *Main Group Chemistry, 23*(1), 17–30. https://doi.org/10.3233/MGC-230067

Kumar, P., Singh, B. K., Pal, B. N., & Pandey, P. C. (2016). Correlation between structural, optical and magnetic properties of Mn-doped ZnO. *Applied Physics A, 122*, 740. https://doi.org/10.1007/s00339-016-0265-7

Kumar, S. S., Kumar, V., Kumar, R., Malyan, S. K., & Pugazhendhi, A. (2019). Microbial fuel cells as a sustainable platform technology for bioenergy, biosensing, environmental monitoring, and other low power device applications. *Fuel, 255*, Article 115682. https://doi.org/10.1016/j.fuel.2019.115682

Li, S., Hu, Y., Xu, Q., Sun, J., Hou, B., & Zhang, Y. (2012). Iron- and nitrogen-functionalized graphene as a non-precious metal catalyst for enhanced oxygen reduction in an air-cathode microbial fuel cell. *Journal of Power Sources, 213*, 265–269. https://doi.org/10.1016/j.jpowsour.2012.04.002

Li, M., Zhou, S., & Xu, M. (2017). Graphene oxide supported magnesium oxide as an efficient cathode catalyst for power generation and wastewater treatment in single chamber microbial fuel cells. *Chemical Engineering Journal, 328*, 106–116. https://doi.org/10.1016/j.cej.2017.07.031

Lv, X., Hong, P., Wen, J., Ma, Y., Spataru, C., & Weng, Y. (2025). Highly efficient operation of an innovative SOFC powered all-electric ship system using quick approach for ammonia to hydrogen. *Frontiers in Energy, 19*(3), 365–381. https://doi.org/10.1007/s11708-025-0974-8

Ma, Y., Wang, B., Wang, H., Zhao, X., Zhao, Y., Wu, S., & Xie, C. (2025). Microstructure regulation and photocatalytic H_2 evolution mechanism of novel MCNTs-Zn0.3Cd0.7S/Pd composites. *International Journal of Hydrogen Energy, 126*, 484–495. https://doi.org/10.1016/j.ijhydene.2025.03.364

Morozov, I., Belousova, O. V., Ortega, D., Mafina, M.-K., & Kuznetcov, M. V. (2015). Structural, optical, XPS and magnetic properties of Zn particles capped by ZnO nanoparticles. *Journal of Alloys and Compounds, 633*, 237–245. https://doi.org/10.1016/j.jallcom.2015.01.285

Nabil, K., Abd-Elrahman, N. A. H., Basfer, N. M., Al-Hadeethi, Y. A., & Umar, S. A. (2022). Applications of Nanomaterials in Microbial Fuel Cells: A Review. *Molecules, 27*, 7483. https://doi.org/10.3390/molecules27217483

Naiel, B., Fawzy, M., Halmy, M. W. A., & Mahmoud, A. E. D. (2022). Green synthesis of zinc oxide nanoparticles using Sea Lavender (*Limonium pruinosum* L. Chaz.) extract: Characterization, evaluation of anti-skin cancer, antimicrobial and antioxidant potentials. *Scientific Reports, 12*, Article 20370. https://doi.org/10.1038/s41598-022-24805-2

Naseer, M., Aslam, U., Khalid, B., & Chen, B. (2020). Green route to synthesize zinc oxide nanoparticles using leaf extracts of *Cassia fistula* and *Melia azadarach* and their antibacterial potential. *Scientific Reports, 10*, 9055. https://doi.org/10.1038/s41598-020-65949-3

Nithya, R., Ragupathy, S., Sakthi, D., Arun, V., & Kannadasan, N. (2020). A study on Mn doped ZnO loaded on CSAC for the photocatalytic degradation of brilliant green dye. *Chemical Physics Letters, 755*, Article 137769. https://doi.org/10.1016/j.cplett.2020.137769

Pandit, S., & Das, D. (2018). Principles of Microbial Fuel Cell for the Power Generation. In D. Das (Ed.), *Microbial Fuel Cell* (pp. 21–41). Springer International Publishing. https://doi.org/10.1007/978-3-319-66793-5_2

Pema, T., Kumar, A., Tripathi, B., Pandit, S., Chauhan, S., Singh, S., Dikshit, P. K., Mathuriya, A. S., Gupta, P. K., & Lahiri, D. (2023). Investigating the performance of lithium-doped bismuth ferrite [BiFe1- xLixO3]-graphene nanocomposites as cathode catalyst for the improved power output in microbial fuel cells. *Catalysts, 13*(3), 618.

Rahman, F., MajedPatwary, M. A., Bakar Siddique, M. A., Bashar, M. S., Haque, M. A., Akter, B., Rashid, R., Haque, M. A., & Royhan Uddin, A. K. (2022). Green synthesis of zinc oxide nanoparticles using Cocos nucifera leaf extract: Characterization, antimicrobial, antioxidant and photocatalytic activity. *Royal Society Open Science, 9*, 220858. https://doi.org/10.1098/rsos.220858

Raizada, P., Sudhaik, A., Patial, S., Hasija, V., Parwaz Khan, A. A., Singh, P., Gautam, S., Kaur, M., & Nguyen, V.-H. (2020). Engineering nanostructures of CuO-based photocatalysts for water treatment: Current progress and future challenges. *Arabian Journal of Chemistry, 13*, 8424–8457. https://doi.org/10.1016/j.arabjc.2020.06.031

Raj, A., & Lawerence, R. (2018). Green synthesis and charcterization of ZnO nanoparticles from leafs extracts of *Rosa indica* and its antibacterial activity. *Rasayan Journal of Chemistry, 11*, 1339–1348. https://doi.org/10.31788/RJC.2018.1132009

Sahni, M., Mishra, R. K., Gupta, A., Thapa, B. S., Thakur, A., Khan, A. A., Pandit, S., Sharma, K., Roy, A., Malik, A., & Jadhav, D. A. (2024). Investigating the performance of CoFe2O4@TiO2 nanomaterial as multifunctional cathode catalyst for simultaneous dye degradation and oxygen reduction in microbial desalination cell. *Desalination, 587*, Article 117958. https://doi.org/10.1016/j.desal.2024.117958

Savla, N., Anand, R., Pandit, S., & Prasad, R. (2020). Utilization of nanomaterials as anode modifiers for improving microbial fuel cells performance. *Journal of Renewable Materials, 8*(12), 1581–1605.

Sharma, K., Pandit, S., Thapa, B. S., & Pant, M. (2022). Biodegradation of Congo red using co-culture anode inoculum in a microbial fuel cell. *Catalysts, 12*, 1219.

Shatnawi, M., Alsmadi, A. M., Bsoul, I., Salameh, B., Mathai, M., Alnawashi, G., Alzoubi, G. M., Al-Dweri, F., & Bawa'aneh, M. S. (2016). Influence of Mn doping on the magnetic and optical properties of ZnO nanocrystalline particles. *Results in Physics, 6*, 1064–1071. https://doi.org/10.1016/j.rinp.2016.11.041

Silambarasan, M., Shanmugam, S., & Soga, T. (2024). Mn-doped ZnO nanoparticles prepared by solution

combustion method. *ResearchGate*. https://doi.org/10.1380/ejssnt.2014.283

Singh Yadav, M., Singh, N., & Bobade, S. M. (2020). Electrochemical analysis of CuO-AC based nanocomposite for supercapacitor electrode application. *Materials Today: Proceedings, 28*, 366–374. https://doi.org/10.1016/j.matpr.2020.02.712

Subha, C., Kavitha, S., Abisheka, S., Tamilarasan, K., Arulazhagan, P., & Rajesh Banu, J. (2019). Bioelectricity generation and effect studies from organic rich chocolaterie wastewater using continuous upflow anaerobic microbial fuel cell. *Fuel, 251*, 224–232. https://doi.org/10.1016/j.fuel.2019.04.052

Talam, S., Karumuri, S. R., & Gunnam, N. (2012). Synthesis, characterization, and spectroscopic properties of ZnO nanoparticles. *ISRN Nanotechnology*. https://doi.org/10.5402/2012/372505

Vemuri, B., Chilkoor, G., Dhungana, P., Islam, J., Baride, A., Koratkar, N., Ajayan, P. M., Rahman, M. M., Hoefelmeyer, J. D., & Gadhamshetty, V. (2022). Oxygen reduction reaction with manganese oxide nanospheres in microbial fuel cells. *ACS Omega, 7*(14), 11777–11787. https://doi.org/10.1021/acsomega.1c06950

Votat, S., Pontié, M., Jaspard, E., & Lebrun, L. (2024). Crystal violet (CV) biodegradation study in a dual-chamber fungal microbial fuel cell with *Trichoderma harzianum*. *Energies, 17*, 247.

Zhang, Z., Crabbe, M. J. C., Bezzeghoud, M., Chen, M., & Turan, V. (2025). Editorial: Climate and environmental changes in circum-Mediterranean regions. *Frontiers in Earth Science*. https://doi.org/10.3389/feart.2025.1594165

Zhao, C., Song, Y., Chen, H., Chen, H., Li, Y., Lei, A., Wu, Q., & Zhu, L. (2025). Improving the performance of microbial fuel cell stacks via capacitive-hydrogel bioanodes. *International Journal of Hydrogen Energy, 97*, 708–717. https://doi.org/10.1016/j.ijhydene.2024.11.424

Zhu, L., Song, Y., Chen, H., Wang, M., Liu, Z., Wei, X., Zhao, C., & Ai, T. (2025). Optimization of power generation and sewage treatment in stacked pulsating gas-liquid-solid circulating fluidized bed microbial fuel cell using response surface methodology. *International Journal of Hydrogen Energy, 101*, 161–172. https://doi.org/10.1016/j.ijhydene.2024.12.397

Publisher's Note Springer Nature remains neutral with regard to jurisdictional claims in published maps and institutional affiliations.